

# Development of a murine iliac arteriovenous fistula model for examination of hemodialysis access-related limb pathophysiology

Kyoungrae Kim, PhD,<sup>a</sup> Erik M. Anderson, MD,<sup>b,c</sup> Andrew J. Martin, MD,<sup>b,c</sup> Qiongyao Hu, BS,<sup>b,c</sup> Tomas A. Cort, BS,<sup>a</sup> Kenneth C. Harland, BS,<sup>b,c</sup> Kerri A. O'Malley, PhD,<sup>b,c</sup> Guanyi Lu, MD, PhD,<sup>b</sup> Scott A. Berceci, MD, PhD,<sup>b,c</sup> Terence E. Ryan, PhD,<sup>a,d</sup> and Salvatore T. Scali, MD,<sup>b,c</sup> Gainesville, Fla

## ABSTRACT

**Objective:** Hemodialysis access-related hand dysfunction is a common clinical feature of patients with chronic kidney disease (CKD) after arteriovenous fistula (AVF) placement. The heterogeneity in symptoms and the lack of a predictive association with changes in hemodynamic alterations precipitated by the AVF suggest that other factors are involved in the mechanisms responsible for causing hand and limb dysfunction postoperatively. To the best of our knowledge, no suitable animal models have provided a platform for performing preclinical experiments designed to elucidate the biologic drivers of access-related hand dysfunction. Therefore, our objective was to develop a novel murine AVF model that could be used to study dialysis access-related limb dysfunction.

**Methods:** Male 8-week-old C57BL/6J mice ( $n = 15/\text{group}$ ) were exposed to either an adenine-supplemented diet to induce CKD or casein-based chow (control). Four weeks after the diet intervention, the mice were randomly assigned to receive an iliac AVF ( $n = 10/\text{group}$ ) or sham surgery ( $n = 5/\text{group}$ ) on the left hindlimb. The mice were sacrificed 2 weeks after surgery, and AVF specimens and hindlimb skeletal muscles were collected for further analysis.

**Results:** Before AVF or sham surgery, the glomerular filtration rates were significantly reduced and the blood urea nitrogen levels were significantly elevated in the CKD groups compared with the controls ( $P < .05$ ). AVF surgery was associated with an  $\sim 80\%$  patency rate among the survivors (four control and three CKD mice died postoperatively). Patency was verified by changes in hemodynamics using Doppler ultrasound imaging and altered histologic morphology. Compared with sham surgery, AVF surgery reduced ipsilateral hindlimb perfusion to the tibialis anterior muscle (20%-40%) and paw (40%-50%), which remained stable until euthanasia. Analysis of gastrocnemius muscle mitochondrial respiratory function uncovered a significant decrease (40%-50%) in mitochondrial function in the AVF mice. No changes were found in the muscle mass, myofiber cross-sectional area, or centrally nucleated fiber proportion in the extensor digitorum longus and soleus muscles between the sham and AVF mice.

**Conclusions:** The results from the present study have demonstrated that iliac AVF formation is a practical animal model that facilitates examination of hemodialysis access-related limb dysfunction. AVF surgery produced the expected hemodynamic changes, and evaluation of the limb muscle revealed a substantial mitochondrial impairment that was present without changes in muscle size. (*JVS—Vascular Science* 2021;2:247-59.)

**Clinical Relevance:** Autogenous arteriovenous fistula creation remains the preferred vascular access option for patients requiring chronic hemodialysis therapy. However, access-related hand dysfunction (ARHD) remains highly prevalent in this population. Clinical management of the disability is difficult because of symptom heterogeneity and limited treatment options. Additionally, the current preclinical models do not adequately replicate the pathologic condition to allow for investigation of underlying mechanisms and to test new therapies. Therefore, medical progress has been marginal. In the present study, we have outlined a novel murine model to study ARHD and described the associated mitochondrial impairments, providing a unique tool for preclinical therapeutic development.

**Keywords:** Arteriovenous fistula; Hand dysfunction; Hemodialysis; Mitochondria; Venous hypertension

More than 550,000 people in the United States have end-stage renal disease requiring chronic renal replacement therapy.<sup>1</sup> It has been estimated that

30% to 60% of the hemodialysis population will develop some element of access-related hand dysfunction (ARHD), which is a spectrum of disease ranging

From the Department of Applied Physiology and Kinesiology,<sup>a</sup> Division of Vascular Surgery and Endovascular Therapy,<sup>b</sup> and Center for Exercise Science,<sup>d</sup> University of Florida; and the Malcolm Randall Veteran Affairs Medical Center.<sup>c</sup>

The present study was supported by the National Institutes of Health (grant R01HL148597 to S.T.S.). Additional salary support was also provided by the National Institutes of Health (grant R01DK119274 to S.A.B. and grant R01HL149704 to T.E.R.).

Author conflict of interest: none.

Correspondence: Salvatore T. Scali, MD, Division of Vascular Surgery and Endovascular Therapy, University of Florida, PO Box 100128, Gainesville, FL 32610 (e-mail: [salvatore.scali@surgery.ufl.edu](mailto:salvatore.scali@surgery.ufl.edu)).

The editors and reviewers of this article have no relevant financial relationships to disclose per the *JVS—Vascular Science* policy that requires reviewers to decline review of any manuscript for which they may have a conflict of interest. 2666-3503

Copyright © 2021 by the Society for Vascular Surgery. Published by Elsevier Inc. This is an open access article under the CC BY-NC-ND license (<http://creativecommons.org/licenses/by-nc-nd/4.0/>). <https://doi.org/10.1016/j.jvssci.2021.09.022>

from subtle paresthesia and neuromotor discoordination to severe monoparesis and digital gangrene.<sup>2</sup> The pathophysiologic mechanisms responsible for ARHD are poorly understood. Historically, the associations between hemodynamic perturbations and limb outcomes have been the focus of studies. However, changes in limb and hand perfusion have not been predictive of the measured clinical changes in hand function.<sup>2</sup>

Other plausible factors that might contribute to the development of ARHD include complex interactions between the hemodynamic alterations precipitated by the vascular access, the systemic influence of the renal dysfunction milieu, and the consequence of highly prevalent comorbidities, such as diabetes, hypertension, and cardiovascular disease.<sup>3,4</sup> Related to neuromotor dysfunction, we have previously described the myopathic and mitochondrial impairments associated with chronic renal insufficiency in mice, principally due to uremic toxin accumulation.<sup>5-7</sup> We also found uremia to significantly exacerbate limb pathology after the severe hemodynamic changes induced by femoral artery ligation.<sup>5</sup> Emerging evidence from human studies support the idea that chronic kidney disease (CKD) contributes to uremic myopathy, including mitochondrial dysfunction.<sup>5,8-10</sup> These observations have raised the intriguing two-hit hypothesis that ARHD might be related to the preexisting neuromuscular pathology caused by uremia toxicity, which, when coupled with the hemodynamic stressor encountered by AVF placement, leads to the observed clinical spectrum of hand dysfunction.

To the best of our knowledge, no reliable preclinical model has been established to allow the investigation of the underlying mechanisms of ARHD. Established preclinical models involve aortocaval and carotid–jugular fistula models, which have typically been used to explore the hemodynamic changes and vascular remodeling associated with arteriovenous fistula (AVF) creation.<sup>11-19</sup> However, because of the anatomic location of these models, the assessment of limb dysfunction is not possible. Furthermore, the preclinical models currently used to study the effects of hemodynamic changes in the hindlimb, such as femoral artery ligation, are limited in their utility because they do not replicate the physiologic conditions of dialysis access surgery, resulting in a different type and degree of ischemic insult. Specifically, the local (ie, steal-associated flow reversal and ischemia, adaptive vascular dilation and remodeling, and venous hypertension) and systemic (ie, decreased peripheral vascular resistance, increased cardiac output, increased venous return, and associated neurohumoral responses) influences after AVF surgery are not re-created in femoral artery ligation models, which, instead, induce an occlusive disease state.<sup>5,20,21</sup> Because of these limitations, a paucity of mechanistic studies has been designed to

## ARTICLE HIGHLIGHTS

- **Type of Research:** A mouse model study
- **Key Findings:** In the present study, we have described the development of a novel murine iliac arteriovenous fistula model that facilitates investigation of hemodialysis access-related limb pathophysiology. Arteriovenous fistula (AVF) placement precipitated hemodynamic perturbations characterized by a measurable reduction in ipsilateral limb perfusion. Hindlimb skeletal muscle mitochondrial dysfunction was a key feature that occurred distally to the AVF without demonstrable muscular injury.
- **Take Home Message:** The murine iliac AVF model provides a new experimental tool that facilitates studies examining the mechanisms of hemodialysis access-related limb pathophysiology and studies evaluating novel therapeutics in a preclinical setting.

treat and/or prevent ARHD, which largely explains why the fundamental understanding of this problem has remained elusive. Therefore, the objective of the present study was to develop a novel murine model capable of examining hemodialysis access-related limb pathophysiology. We have described the creation and validation of an iliac AVF model and assessed the associated hindlimb myopathy and pathophysiology in mice with and without chronic renal insufficiency.

## METHODS

**Mice.** Male 8-week-old C57BL/6J mice ( $n = 30$ ) were purchased from Jackson Laboratory (Bar Harbor, Me) and housed in a light (12:12-hour light/dark cycle), humidity (~50%), and temperature (~22°C) controlled room. The mice were provided either a casein-based control diet or an adenine-supplemented diet to induce chronic renal insufficiency, as previously described.<sup>5,6,22</sup> Four weeks after starting the diet interventions, the control and CKD mice were randomly allocated to undergo either AVF ( $n = 10$ /group) or sham ( $n = 5$ /group) surgery. This initial validation of the iliac AVF model was performed using only male mice because young female mice are known to display less pathologic susceptibility to surgical and diet-induced renal disease models.<sup>6,23-25</sup> However, it is important that future studies examine this AVF model in female mice with renal insufficiency because ARHD is often experienced by female patients with CKD.<sup>26</sup> All animal experiments adhered to the Guide for the Care and Use of Laboratory Animals from the Institute for Laboratory Animal Research (National Academy Press, National Research Council, Washington, DC, 1996) and any updates. The institutional animal care and use committee of the University of Florida and Malcom Randall Veterans Affairs Medical Center approved all procedures.

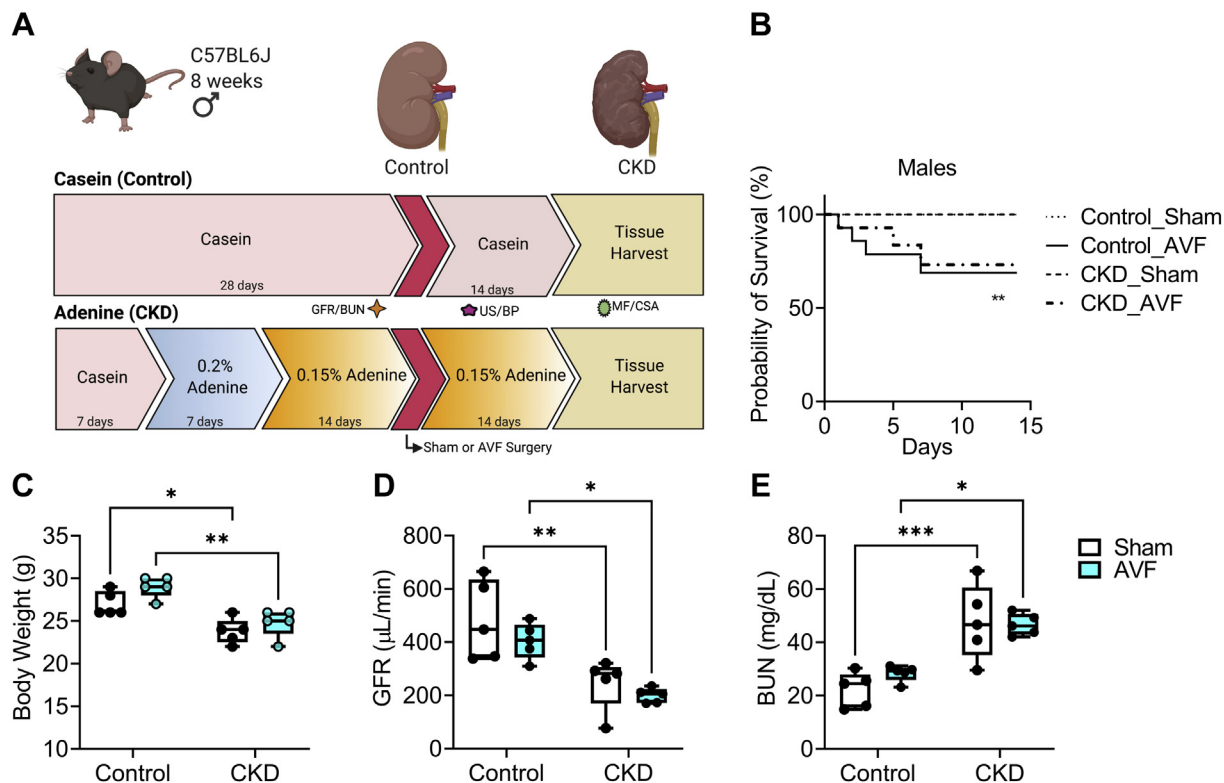


**Fig 1.** Schematic of iliac arteriovenous fistula (AVF) creation. Graphic description of the surgical steps for the construction of an iliac AVF on the left hindlimb. **A**, A midline laparotomy was made once the mouse was anesthetized. **B**, Next, 4-0 sutures were placed on the proximal and distal iliac vascular bundles and rotated clockwise. **C**, A longitudinal venotomy ( $\sim 1$  mm) was made on the anterior wall of the iliac vein. **D**, An imbricating 10-0 silk suture was placed through the posterior wall of the iliac vein and the anterior wall of the iliac artery. **E**, Approximately  $0.8 \times 0.3$ -mm elliptical incision was made to create the arteriovenous anastomosis. **F**, The initial anterior wall venotomy was closed using 10-0 silk sutures.

**Assessment of renal function.** Three to five days before surgery, renal function was evaluated by measuring the glomerular filtration rate (GFR) via fluorescein isothiocyanate-labeled inulin clearance, as previously described.<sup>5,6,27,28</sup> Blood urea nitrogen was determined using a commercial kit (model no. KO24; Arbor Assays, Ann Arbor, Mich) according to the manufacturer's instructions.

**Iliac AVF creation.** The construction of an AVF between the common iliac artery and vein was performed in mice at 12 weeks of age. Once the mice had been adequately anesthetized with isoflurane and placed in a supine position, a midline laparotomy was made from the lower edge of the costal margin to the pubis (Fig 1, A). After abdominal exploration, the left common iliac artery and vein bundle was carefully dissected from the surrounding retroperitoneal tissues. However, care was taken not to separate the two vessels, because they are naturally and intimately adherent in vivo. Next, 4-0 sutures were placed on the proximal and distal vascular bundle (iliac artery/vein)  $\sim 4$  mm apart to serve as vessel cross-clamps. Once the left iliac artery and vein bundle had been isolated and controlled by these 4-0 sutures using single

knot ligatures, they were axially rotated (clockwise) anteriorly such that the iliac vein was anterior to the iliac artery (Fig 1, B). Next, a longitudinal venotomy ( $\sim 1$  mm) was made on the left iliac vein (Fig 1, C). An imbricating 10-0 silk suture was placed through the posterior wall of the iliac vein that was in immediate apposition to the anterior wall of the iliac artery (Fig 1, D). This was performed to displace the anterior wall from the posterior wall of the iliac artery with gentle tension. An elliptical incision,  $\sim 0.8 \times 0.3$  mm, was then made through the common iliac vein–artery walls to create the arteriovenous anastomosis, followed by removal of the imbricating sutures (Fig 1, E). A 0.9% sodium chloride solution was used to flush the vessels and prevent clot formation. The initial anterior wall venotomy on the iliac vein was then closed using interrupted 10-0 suture to complete creation of the AVF (Fig 1, F). The 4-0 single-knot ligature sutures were then removed from distally to proximally, and hemostasis was confirmed. Pulsatile flow of oxygenated blood within the iliac vein and inferior vena cava (IVC) provided immediate visual feedback regarding the technical success of the AVF. The midline incision was closed with 5-0 absorbable suture in a simple continuous pattern. The mice were allowed to

recover on a warming pad and given subcutaneous injections of buprenorphine (~0.1 mg/kg) for pain control and subcutaneous normal saline resuscitation for 48 hours postoperatively. The mice assigned to sham surgery also underwent the same surgical procedures, including dissection of the left iliac vasculature and temporary (~20 minutes) ligation of the proximal iliac artery and vein but without AVF creation. The timing of the iliac vessel cross-clamping for the sham surgery was matched to that of the AVF mice.

**High-frequency duplex ultrasound imaging.** The anatomy and flow velocities of the infrarenal aorta, IVC, and bilateral iliac vessels were measured pre- and postoperatively using duplex ultrasound. The Vevo 2100 Imaging System (VisualSonics, Inc, Toronto, Ontario, Canada) with an MS-550D (40-MHz) MicroScan transducer (VisualSonics, Inc) was used for imaging. The imaging studies were acquired with the mice under general anesthesia. Preoperative imaging was obtained 1 day before AVF surgery, and postoperative imaging was obtained on postoperative days 3 and 13 to verify AVF patency throughout the experimental period. B-mode imaging was initially used to identify the vascular anatomic landmarks, followed by color and pulse-wave Doppler interrogation of the individual vessels. A 60° angle of insonation was used for all velocity measurements.

**Histologic assessment of fistula formation.** On the sacrifice date, each mouse was anesthetized with isoflurane. After procurement of the extensor digitorum longus (EDL), soleus, and gastrocnemius muscles, a midline incision was made to expose the left iliac vascular bundle, which was separated from the surrounding retroperitoneal fat and connective tissues. Once this anatomic isolation was completed, the thorax was opened, the IVC was severed, and 10 mL of 0.9% normal saline, followed by 10 mL of 10% neutral buffered formalin, was perfused through the left ventricle. At ~30 minutes after fixation, the left common iliac artery and vein bundle was ligated proximally and distally using two 4-0 silk sutures with orientation markers in place for mounting. Next, the vascular bundle was excised en bloc, transferred to a cassette, and set in a small container filled with 10% neutral buffered formalin for 48 to 72 hours at room temperature. After dehydration in 70% ethanol and clearing in xylene, the specimen was embedded in paraffin, chilled on an ice block (Tissue-Tek Cryo Console; Sakura Finetek, Torrance, Calif), and serial transverse sections (5 µm thickness) were cut from proximal to distal sites using a Microm HM 315 microtome (Microm GmbH, Dreieich, Germany). Every 10th section was mounted on labeled slides and subsequently stained with Masson's trichrome. Images were acquired using an optical microscope (Zeiss, Oberkochen, Germany) connected to an

Infinity 3 camera (Lumenera Scientific, Ottawa, Ontario, Canada).

**Assessment of hindlimb perfusion.** Hindlimb perfusion was measured using a laser Doppler flowmeter (moorVMS-LDF; Moor Instruments, Wilmington, Del) 1 day before and 0, 3, 7, and 13 days after AVF surgery. Under isoflurane anesthesia, the mice were placed on a water-circulating pad at 37°C, and the leg hair was shaved using a pen trimmer. Once the mouse's breathing pattern was stable, the laser Doppler probe was placed against the skin of the tibialis anterior muscle and the plantar skin proximal to the footpad to determine the peripheral tissue blood flow. The data were collected for 30 seconds, and the average values were used for analysis. Limb perfusion was calculated by the proportional changes in perfusion relative to the contralateral limb.

**Preparation of mitochondrial isolation.** The skeletal muscle mitochondria were isolated as previously described.<sup>7,29</sup> After dissection, the left gastrocnemius muscle was placed in mitochondrial isolation medium (300 mM sucrose, 10 mM HEPES, and 1 mM EGTA; pH, 7.1). After removing excess blood, connective tissue, and fat, the muscle was minced, placed in ice-cold mitochondrial isolation medium supplemented with 1 mg/mL bovine serum albumin (BSA), homogenized on ice using a glass-Teflon homogenizer (Wheaton) at ~3500 rpm and centrifuged at 800g for 10 minutes. The resulting supernatant was transferred to a new prechilled tube and centrifuged at 10,000g for 10 minutes to collect the mitochondrial pellet. All steps were processed at 4°C. The mitochondrial pellet was gently washed to remove any damaged mitochondria and then resuspended in mitochondrial isolation medium, and the protein concentration was determined using a bicinchoninic acid protein assay (model SL256970; Thermo Fisher Scientific, Waltham, Mass).

**Measurement of mitochondrial respiratory function.** Mitochondrial respiratory function was assessed using high-resolution respirometry (Oxygraph-2k; Oroboros Instruments, Innsbruck, Austria) by measuring the oxygen flux at 37°C in buffer Z (105 mM K-MES, 30 mM KCl, 1 mM EGTA, 10 mM K<sub>2</sub>HPO<sub>4</sub>, 5 mM MgCl<sub>2</sub>·6H<sub>2</sub>O, and 2.5 mg/mL of BSA; pH, 7.2) supplemented with 20 mM creatine, as previously described.<sup>6,7,29</sup> The following protocol was used to assess mitochondrial respiratory capacity: the addition of 5 mM pyruvate plus 2.5 mM malate as substrates, followed by a bolus of adenosine diphosphate (16 mM), and cytochrome C (0.005 mM) to assess the integrity of the outer mitochondrial membrane. Mitochondrial oxygen consumption was normalized to the amount of mitochondrial protein loaded into the respirometer.

**Immunofluorescence analysis of muscle cross-sectional area.** The myofiber cross-sectional area was analyzed using immunofluorescence microscopy, as described previously.<sup>5,24</sup> In brief, isolated EDL and soleus muscles were mounted in disposable base molds (catalog no. 6235215; Electron Microscopy Sciences, Hatfield, Pa) with embedding medium compound (Tissue-Tek O.C.T; Sakura Finetek, Torrance, Calif) and frozen in liquid nitrogen-cooled isopentane. Serial transverse sections of 10  $\mu$ m were cut from the mid-belly using a Leica 3050S cryostat (Leica Biosystems, Richmond, Ill) at  $-20^{\circ}\text{C}$ , mounted on frosted microscope slides, briefly air dried at room temperature, and stored at  $-80^{\circ}\text{C}$  for subsequent analysis. Frozen muscle sections were air dried at room temperature for 10 minutes, followed by fixation with 4% paraformaldehyde for 5 minutes. After  $1\times$  phosphate-buffered saline (PBS) washes, the sections were permeabilized with 0.3% Triton X-100 (Dow Chemical Co, Midland, Mich) for 10 minutes. After multiple  $1\times$  PBS washes, the sections were incubated in blocking buffer (5% goat serum and 1% BSA in PBS) for 1 hour. Thereafter, the sections were incubated with anti-laminin primary antibody (catalog no. L9393; 1:100; Sigma-Aldrich, St Louis, Mo) overnight at  $4^{\circ}\text{C}$ . After a series of  $1\times$  PBS washes, the muscle sections were labeled with a secondary antibody (Alexa Fluor 488 goat anti-rabbit IgG, 1:250; Thermo Fisher Scientific). After  $1\times$  PBS washes, coverslips were mounted with fluorescent mounting medium (H-1500; Vector Laboratories, Burlingame, Calif). Subsequently, the slides were imaged at  $20\times$  magnification using an Evos FL2 auto microscope (Thermo Fisher Scientific). Quantification of the myofiber cross-sectional area was performed using MuscleJ (ImageJ plugin; National Institutes of Health, Bethesda, Md).<sup>30</sup>

**Histologic analysis of centrally nucleated fibers.** Another set of frozen muscle sections was used for histologic analysis of centrally nucleated fibers, which were stained with hematoxylin and eosin, as previously described.<sup>5</sup> Bright field images of the entire cross section were acquired at  $20\times$  magnification using an Evos FL2 microscope (Thermo Fisher Scientific). The number of fibers with centrally nucleated fibers on the EDL and soleus muscles were manually counted using an ImageJ counting tool (National Institutes of Health), with the result expressed as a proportion of all fibers.

**Statistical analysis.** Data are presented as the mean  $\pm$  standard deviation or using box and whisker plots with 5% to 95% confidence intervals with the individual points presented. The normality of all data was assessed using the Shapiro-Wilk test. Data that were not normally distributed were analyzed using a Kruskal-Wallis test. All the comparisons across the four groups (diet  $\times$  surgery) were performed using a two-way analysis of variance, except for blood perfusion (compared using repeated measures of two-way analysis of variance) with Tukey's post hoc

multiple comparisons when pairwise comparisons were appropriate. Statistical analysis was performed using GraphPad Prism, version 9.0 (GraphPad, San Diego, Calif). In all cases,  $P < .05$  was considered statistically significant.

## RESULTS

A graphic overview of the study design and experimental timeline, including the major outcome measurements, is shown in Fig 2, A. A total of 10 control and 10 CKD male mice had undergone AVF surgery on the left common iliac vessels. Postoperatively, seven mice had died after AVF placement (four control and three CKD mice). Postoperative monitoring was performed at least once daily, and the mice with a deteriorating physical condition were euthanized. However, necropsy to determine the cause of death was not performed. No mortality was reported for the mice assigned to sham surgery ( $n = 5/\text{group}$ ; Fig 2, B). Compared with the control mice, the mean body weight was significantly lower in the mice fed the adenine diet, irrespective of the surgical group (Fig 2, C). As expected, the GFR (Fig 2, C) was significantly reduced and the blood urea nitrogen levels (Fig 2, D) were significantly increased in the CKD mice compared with the casein-fed control mice.

**Ultrasound and histologic assessment of AVF patency.** Doppler ultrasound was used to confirm the presence and patency of the AVF postoperatively on days 3 and 13. During each assessment, arterialized waveforms within the left iliac vein on pulse-wave analysis with high velocity and low resistance patterns (Fig 3, A and B) were indicative of a patent AVF. Alternatively, low velocity waveforms within the vasculature (Fig 3, C) or the lack of any flow were suggestive of thrombosis and technical failure. Direct observation on duplex ultrasound imaging of the iliac arteriovenous connection and turbulent flow on color Doppler ultrasound analysis (Fig 3, D and E) also confirmed the presence of a patent AVF. Patency was also indirectly measured using pulse-wave analysis of the infrarenal aorta and IVC. A successful fistula was found to cause pulsatile blood flow and significantly increased peak systolic velocities in the IVC (Fig 3, F and G), consistent with venous hypertension. Similarly, increased aortic peak systolic velocities and end-diastolic velocities were noted with each patent fistula (Fig 3, H and I), secondary to decreased peripheral vascular resistance.

After sacrifice, histologic examination of left iliac vasculature was used to confirm the ultrasound findings. The morphologic evidence of a successful AVF in serial sections from the proximal to the distal iliac vasculature, stained with Masson's trichrome, is shown in Fig 4, A. Intimal hyperplasia and arterialization with fibrosis were prominent observations of venous remodeling at the proximal and distal sites both. In contrast, the morphologic changes within the artery were subtle. This histologic evidence of the AVF was clearly distinguishable from

## Model

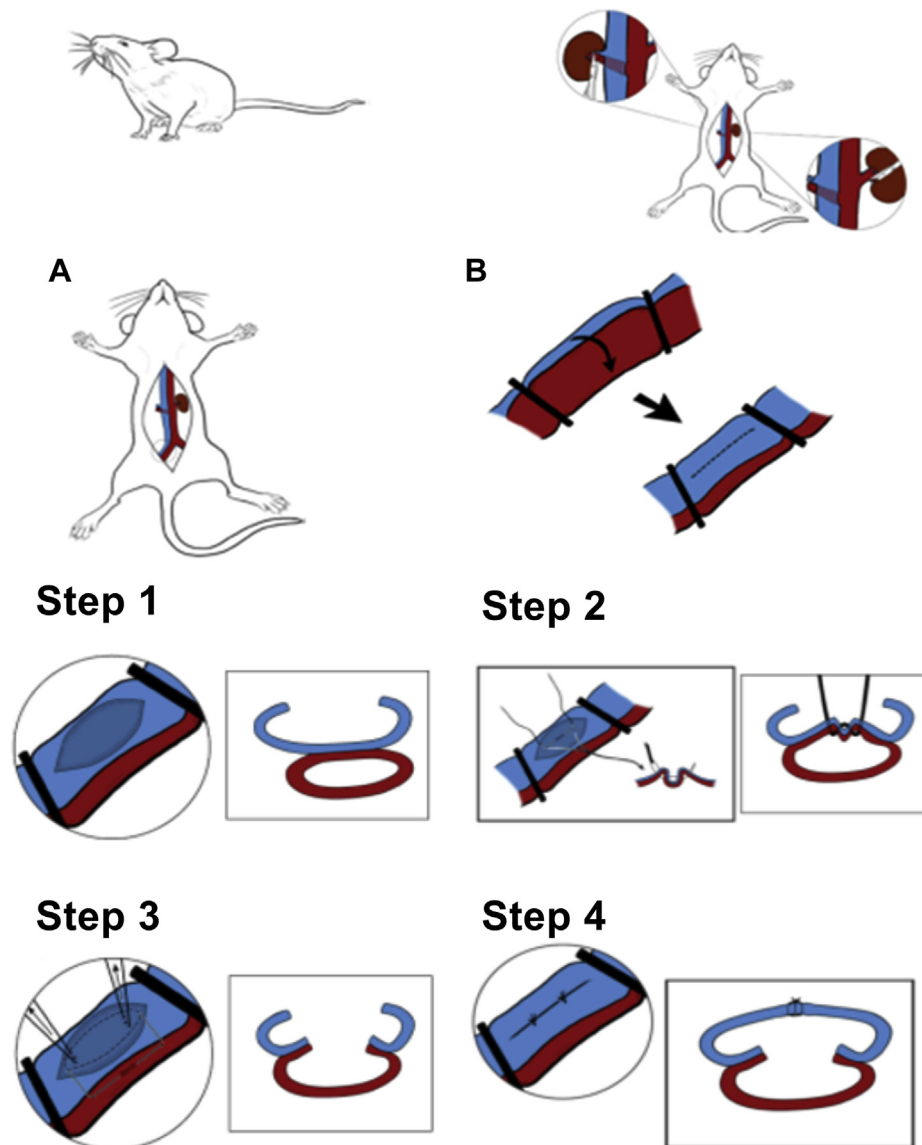


**Fig 2.** Study design and characteristics of renal insufficiency. **A**, Schematic overview of the study design for arteriovenous fistula (AVF) model development using adult male C57BL/6J mice allocated to control (casein diet) and chronic kidney disease (CKD; adenine diet) groups. **B**, Probability of survival after AVF construction. **C**, Body weights for control and CKD mice. **D**, Glomerular filtration rate (GFR) measured by fluorescein isothiocyanate-inulin clearance. **E**, Blood urea nitrogen (BUN) measured using a commercial kit. The GFR and BUN tests were conducted 3 to 5 days before AVF surgery. The data were analyzed using two-way analysis of variance and Tukey's post hoc analysis were performed, as appropriate. *Box and whiskers* represent the mean and 5% to 95% confidence intervals with individual data. \* $P < .05$ , \*\* $P < .01$ , \*\*\* $P < .001$  vs control;  $n = 5$ /group.

the vascular anatomy after sham surgery (Fig 4, B). Fistula histologic examination revealed that one control and two CKD mice, of the survivors that had undergone AVF surgery, had developed thrombosis at the site of the fistula or upper iliac artery stream (Fig 4, C). The cumulative frequencies of AVF patency, thrombosis, and postoperative mortality are shown for the control and CKD mice in Fig 4, D.

**AVF creation reduced hindlimb perfusion.** To evaluate the hemodynamic changes to the ipsilateral hindlimb after AVF creation, we measured the blood perfusion in the tibialis anterior muscle and ventral paw using laser Doppler flowmetry before surgery, 4 hours after surgery, and 3, 7, and 13 days postoperatively. The reduction in limb perfusion relative to the contralateral leg in both the tibialis anterior muscle and paw were similar

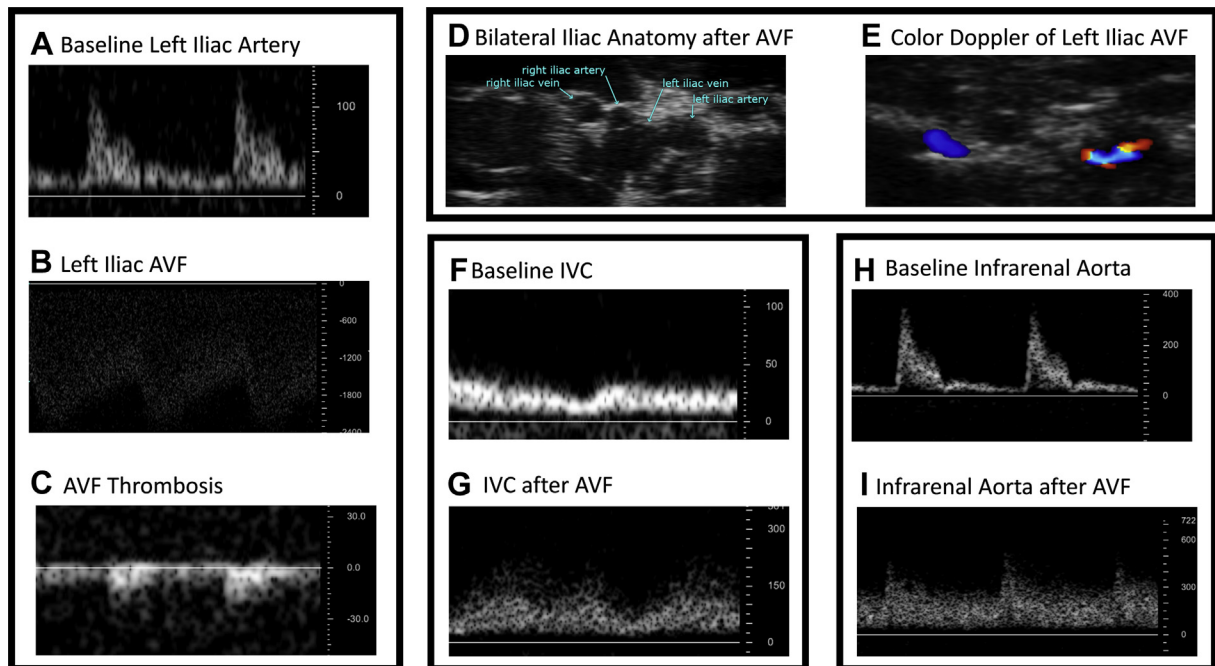


**Fig 3.** Doppler ultrasound confirming the presence of the iliac arteriovenous fistula (AVF). **A**, Baseline left iliac artery pulse-wave Doppler velocity measurements. **B**, Very high velocity pulsatile waveform at the left iliac surgical site consistent with a patent AVF. **C**, Low velocity waveform at the left iliac surgical site consistent with thrombosis and AVF closure. Similarly, a lack of flow within the iliac vasculature (data not shown) consistent with thrombosis. **D**, Bilateral iliac anatomy after successful left iliac AVF creation. Left iliac artery and vein dilation were noted compared with right-sided anatomy. **E**, Color Doppler assessment of a successful AVF with turbulent flow at AVF site. In contrast, laminar flow was noted within the right iliac vasculature. **F**, Baseline inferior vena cava (IVC) monophasic low velocity waveform. **G**, IVC waveform after successful AVF creation with pulsatility and elevated velocity. **H**, Baseline infrarenal aortic waveform. **I**, Infrarenal aortic waveform after successful AVF with elevated peak systolic velocity, severely elevated diastolic velocities, and loss of triphasic waveform. All velocity measurements were millimeters per second.

between the control and CKD mice that had received an AVF ( $P > .05$ ; Fig 5, A and B). The magnitude of the decrease in perfusion was greater in the paw (40%-50%) than in the tibialis anterior muscle (20%-30%). During the 14-day postoperative period, limb perfusion did not recover, suggesting that arteriogenesis and/or collateral vessel development did not occur.

#### AVF placement caused mitochondrial myopathy.

Accumulating evidence from both human and animal studies has suggested that skeletal muscle mitochondrial abnormalities contribute to the myopathic symptoms in CKD.<sup>6,8,9,31-34</sup> Thus, we assessed the mitochondrial respiratory function to determine how renal dysfunction coupled with AVF construction affects muscle mitochondrial health. An overview of the mitochondrial respiratory function protocol used in this experiment is shown in Fig 6, A. First, we energized mitochondria in the absence of adenylates with pyruvate and malate to measure state 2 respiration, which displayed significant diet (CKD) and surgery (AVF) effects (Fig 6, B). Next, maximal state 3 respiration was measured after the addition of 4 mM adenosine diphosphate to assess the maximal respiratory capacity supported by

substrates that provide electrons to complex I, which demonstrated significant mitochondrial impairment in AVF mice (Fig 6, C). Thereafter, exogenous cytochrome C was added to assess the integrity of the outer mitochondrial membrane (Fig 6, D). Finally, the subsequent addition of succinate allowed for additional electrons to enter the electron transport system through complex II (succinate dehydrogenase), facilitating analysis of maximal state 3 respiration supported by complex I+II substrates (Fig 6, E), which also displayed significant diet (CKD) and surgery (AVF) effects. Taken together, these results have confirmed a two-hit phenomenon in which the uremic milieu itself causes muscle mitochondrial impairment, which is exacerbated by the hemodynamic changes resulting from AVF placement.

The mitochondrial impairments shown in Fig 6 occurred without overt changes to the muscle mass (Fig 7, A and B), myofiber size (Fig 7, C and D), or ischemic muscle injury (indicated by the centrally nucleated fibers; Fig 7, E and F) in both fast-twitch (EDL) and slow-twitch (soleus) muscles. To examine the potential relationships between key outcome measures, we implemented Pearson correlation analyses (Fig 8). The results of these analyses revealed strong correlations between the GFR and

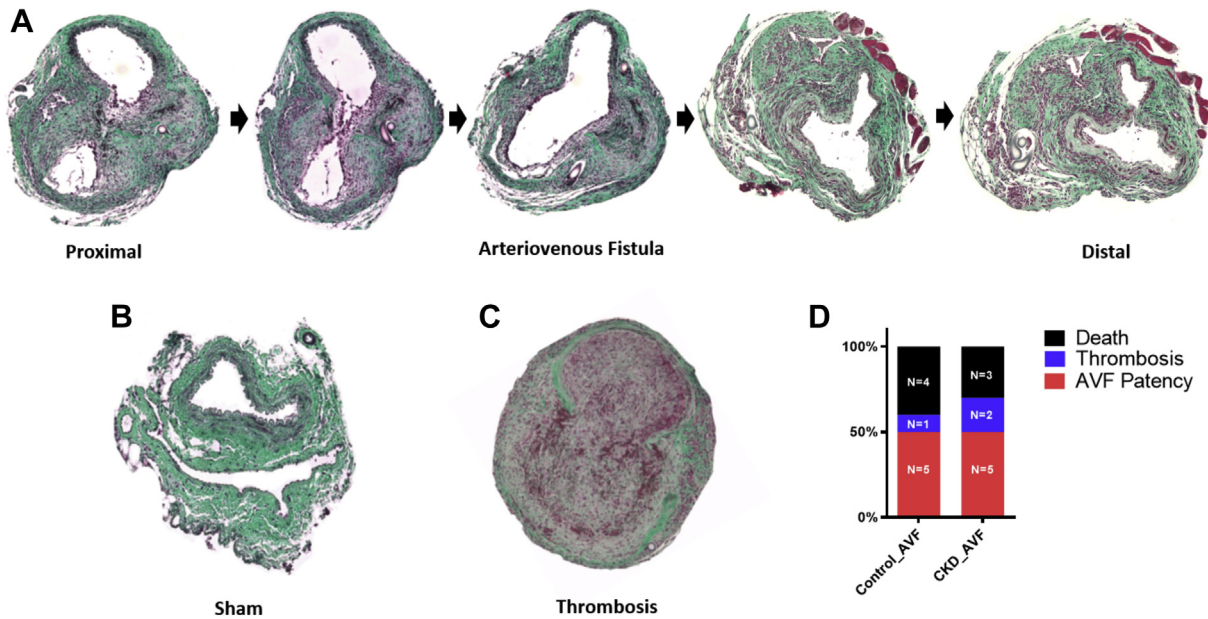


**Fig 4.** Histologic assessment of arteriovenous fistula (AVF) formation. **A–C**, Representative images (10× magnification) of AVF stained with Masson’s trichrome. **A**, A series of cross sections of AVF from the proximal site (left) to the distal site (right), with AVF in the middle image. **B**, A cross section of the middle portion of the arteriovenous bundle from the sham-operated limb. **C**, A representative image of thrombosis development at the site of the AVF. **D**, Proportion and number of AVF patency, thrombosis, and postoperative mortality for mice that had undergone AVF creation.

mitochondrial respiratory capacity ( $P < .05$ ) and postoperative limb perfusion and mitochondrial respiratory capacity ( $P < .05$ ). However, no significant correlation between the GFR and postoperative limb perfusion with mitochondrial respiratory capacity was found ( $P > .05$ ). These correlation analyses suggest that both renal insufficiency and reduced limb muscle perfusion can independently alter muscle mitochondrial health.

## DISCUSSION

Hemodialysis is a life-saving therapy for patients with end-stage renal disease, and autogenous AVF creation remains the preferred vascular access option.<sup>35</sup> ARHD, however, has high prevalence in this population and can present with a variety of signs and symptoms, including numbness, weakness, pain, atrophy, and/or ulceration, resulting in functional deficits that are associated with a poor quality of life.<sup>2,3,36,37</sup> Despite the increasing worldwide incidence of end-stage renal disease and dialysis access surgery, no preclinical model of ARHD is available to define the potential mechanisms responsible for the observed hand and limb disability. In the present study, we have reported the development of an iliac AVF model that facilitates the assessment of limb-associated pathophysiology. This novel model produced clinically relevant limb changes, including hemodynamic alterations, morphologic changes in arteriovenous anatomy, mild peripheral limb ischemia,

and impaired skeletal muscle mitochondrial function without notable atrophy or injury after AVF construction.

To recapitulate the clinical condition, we used the established adenine-induced nephropathy model to induce renal insufficiency before AVF creation.<sup>7,24,38</sup> Compared with the control mice, the mice exposed to the adenine diet had had a smaller body mass and kidney dysfunction consistent with previous reports.<sup>5–7,22</sup> No differences were found in mortality between the control and CKD groups, indicating that the adenine diet-induced nephropathy did not aggravate the surgery-related mortality in this model. This is an important finding that provides a useful option of CKD induction for future animal research because most previous AVF studies have used either mice with normal kidney function or mice subjected to the 5/6 nephrectomy, which on its own has a significant mortality rate.<sup>12,16,18,39–43</sup>

A suitable preclinical model of AVF should possess several key aspects, in particular, fistula patency and/or maturation, throughout the experimental time course. Because the primary goal for AVF construction clinically is to secure a functional and long-lived vascular access for hemodialysis, most animal studies have focused primarily on the vascular remodeling or hemodynamics associated with fistula patency and/or maturation.<sup>12,14,18,19,39,44</sup> In the present study, the results revealed 50% patency in the iliac AVF model with 30% postoperative mortality and a 20% rate of thrombosis that resulted in closure of the AVF. In all cases,

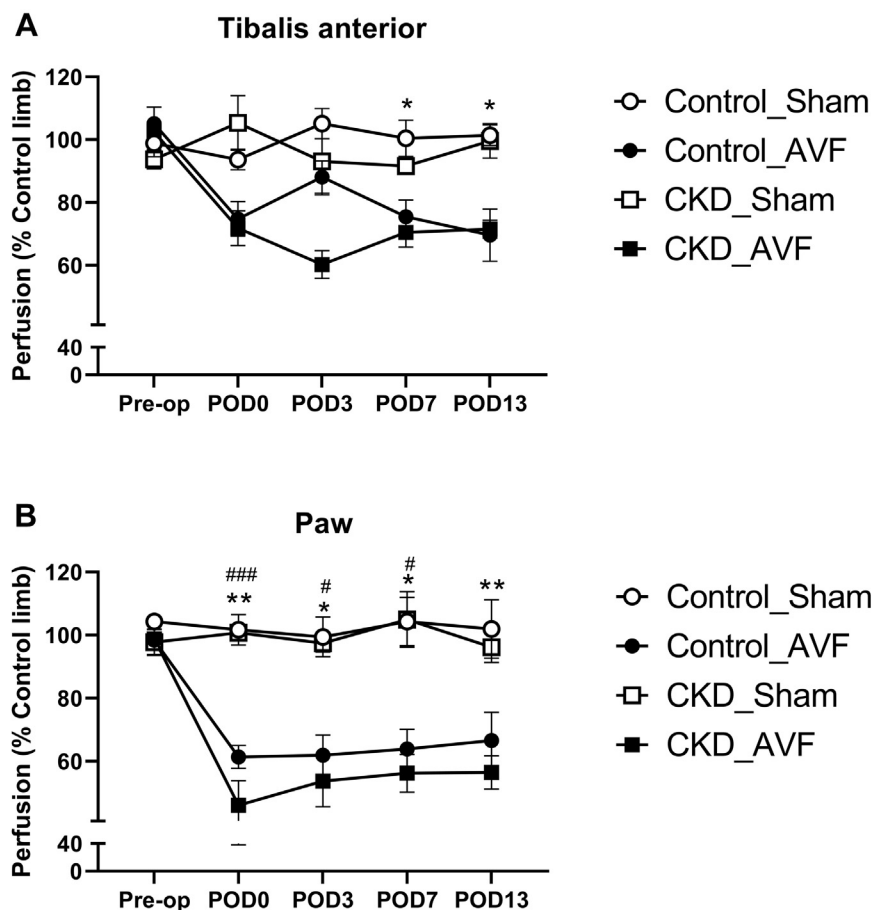


**Fig 5.** Laser Doppler limb perfusion demonstrating hemodynamic changes in the hindlimb. Limb perfusion to the tibialis anterior muscle (A) and ventral paw (B) before and after arteriovenous fistula (AVF) formation and 3, 7, and 13 days after surgery. Data were analyzed using a repeated measures of two-way analysis of variance and Tukey's post hoc analysis were performed, as appropriate. Data presented as mean  $\pm$  standard deviation. CKD\_Sham vs CKD\_AVF: \* $P < .05$ , \*\* $P < .01$ ; CON\_Sham vs CON\_AVF: # $P < .05$ , ### $P < .01$ , #### $P < .001$ ;  $n = 5/\text{group}$ . POD, Postoperative day; Pre-op, preoperative.

closure of the AVF was detectable by ultrasound as early as 3 days after surgery, with a lack of flow or very low velocity waveforms within the vasculature (Fig 3, C) observed. For the successful patent fistula, we confirmed access-induced hemodynamic changes, including a dilated inflow artery and outflow vein, venous hypertension, and pulsatile fistula flow with spectral broadening. We also visually inspected the anastomosis and blood mixture at the site of the AVF (Fig 3, E). In addition, the histologic analysis of the iliac AVFs, processed with Masson's trichrome staining, revealed a series of morphologic changes in response to AVF creation (Fig 4, A). In agreement with previous studies, compared with the sham-operated limb, we detected distinct outflow venous intimal hyperplasia and smooth muscle layer thickening at 2 weeks after AVF creation.<sup>16,18,39,40</sup> Thrombosis was noted on histologic examination in  $\sim 20\%$  of the mice that had undergone AVF surgery. This finding corresponded well with the ultrasound imaging findings of failure. These results

suggest that ultrasound imaging studies and histologic examination techniques will be sufficient to determine AVF functionality and longevity. Thus, noninvasive, short (5-10 minutes) inspections of fistula patency using ultrasound might be a useful tool for determining early exclusion in future preclinical studies.

One of the most notable pathologic changes associated with ARHD is the reduction in extremity perfusion, known as "steal syndrome."<sup>37</sup> A reduction in limb pressures has been found in  $\leq 80\%$  of brachial-based procedures, although cases with severe symptoms requiring aggressive surgical intervention have been relatively low ( $\sim 10\%$ ).<sup>2</sup> Although the degree to which the hemodynamics change after AVF placement might not directly correlate with the spectrum of observed clinical symptoms, understanding the perfusion changes related to dialysis-access surgery is important because these could be associated with peripheral neuropathy.<sup>45-48</sup> In the present study, we found significant decreases in hindlimb perfusion immediately after AVF creation that

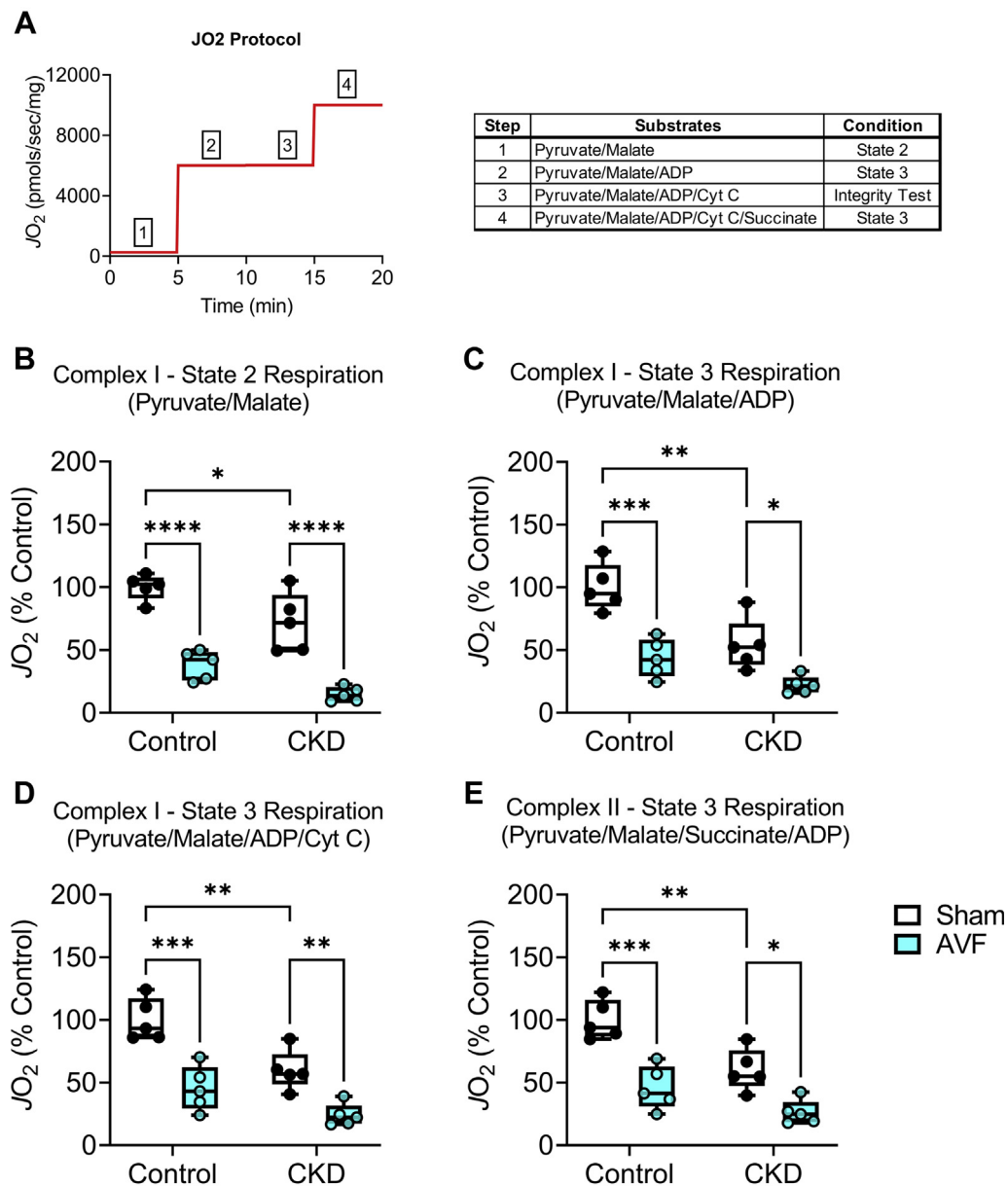


**Fig 6.** Skeletal muscle mitochondrial respiratory function was impaired after arteriovenous fistula (AVF) placement. Gastrocnemius muscle mitochondria was isolated from control and chronic kidney disease (CKD) mice that had undergone sham or AVF surgery. **A**, Graphic depiction of detailed respiratory protocol used. **B**, State 2 respiration supported by pyruvate and malate. **C**, Adenosine diphosphate (ADP)-stimulated mitochondrial respiration supported by pyruvate and malate. **D**, State 3 respiration after addition of cytochrome C, which was used for mitochondrial integrity check. **E**, State 3 respiration supported by pyruvate, malate, and succinate. Data were analyzed using two-way analysis of variance, and Tukey's post hoc analysis was performed, as appropriate. Box and whiskers represent the mean and 5% to 95% confidence intervals with individual data. \* $P < .05$ , \*\* $P < .01$ , \*\*\* $P < .001$ , \*\*\*\* $P < .0001$  vs Sham; # $P < .05$ , ## $P < .01$  vs CKD;  $n = 5$ /group. Cyt C, Cytochrome C;  $JO_2$ , Mitochondrial respiratory oxygen flux.

persisted throughout the 14-day postoperative period (Fig 5). The magnitude of reduction was greater in the distal paw (~45% reduction) than that in the more proximal tibialis anterior muscle (~30% reduction). An increasing body of evidence has supported the notion that peripheral limb ischemia, followed by oxidative stress, can lead to skeletal muscle pathology, including

mitochondrial abnormalities and muscle injuries in both clinical and preclinical studies.<sup>5,49,50</sup> In alignment with these findings and compared with the results from the sham mice, the AVF mice had severe impairments in mitochondrial function (Fig 6). Similar to our previous study, we also found that adenine diet-induced nephropathy alone had negative effects on

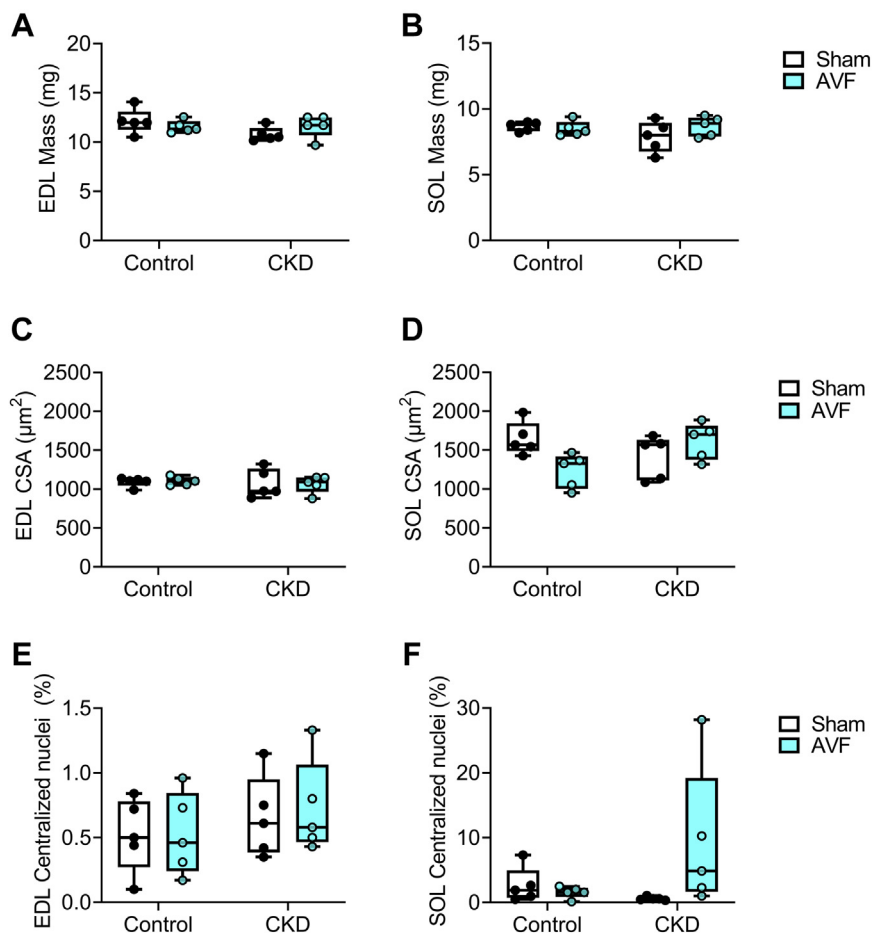


**Fig 7.** Hindlimb skeletal muscle mass, fiber cross-sectional area, and centrally nucleated fibers with arteriovenous fistula (AVF) placement. **A**, Muscle mass for the extensor digitorum longus (EDL) muscle. **B**, Muscle mass for the soleus (SOL) muscle. **C**, Myofiber cross-sectional area (CSA) of EDL muscle measured via laminin-stained transverse sections. **D**, Myofiber CSA of the SOL muscle measured via laminin-stained transverse sections. **E**, Proportion of centrally nucleated fibers in EDL cross section stained with hematoxylin and eosin. **F**, Proportion of centrally nucleated fibers in SOL cross section stained with hematoxylin and eosin. Data were analyzed using a two-way analysis of variance and Tukey's post hoc analysis were performed, as appropriate. *Box* and *whiskers* represent the mean and 5% to 95% confidence intervals with individual data (n = 5/group).

mitochondrial function.<sup>6,7,24</sup> The correlation analyses identified significant relationships between GFR or hindlimb perfusion and mitochondrial function, reinforcing the independent effects of renal insufficiency and hemodynamic changes on muscle mitochondrial health. These findings have set the stage for future studies to test preclinical therapeutics to mitigate mitochondrial myopathy resulting from independent uremic toxicity and/or ischemic insult or comorbid effects. However, we found no overt ischemic muscle injury or atrophy despite the clear presence of mild limb ischemia. Several clinical studies have suggested that ischemia-induced muscle injury might require a higher threshold than access-related shunting.<sup>45,47,48</sup>

One limitation of the present study might have been the insufficient study period. Many patients with ARHD will experience acute onset of symptoms after

access creation, often requiring prompt intervention, which matches the pathology described in our model. However, a subset of patients will experience delayed or progressive symptoms. Vascular remodeling and physiologic maturation might play a role in the pathogenesis and hemodynamics in this chronic presentation. Although duplex ultrasound imaging showed hemodynamic characteristics of a patent AVF in this model, flow-mediated changes have not been characterized over time. Similarly, the characteristics of limb functional impairment have not been qualified in our model as they relate to AVF creation and the associated myopathy. Future directions for this model should consider longitudinal ultrasound assessments of the vascular diameter and flow-related changes and characterization of limb functional assessments during the study period.

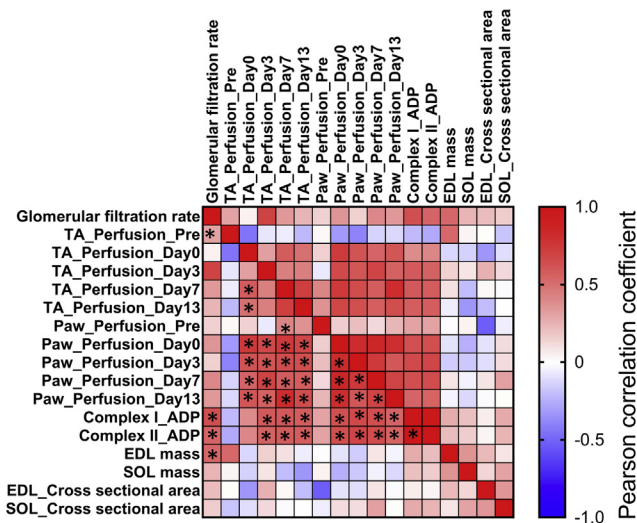


**Fig 8.** Results from Pearson correlation analyses across the outcome measurements. Pearson correlation coefficients between glomerular filtration rate (GFR), hindlimb blood flow, skeletal mitochondrial respiratory function, and muscle mass and cross-sectional area (CSA) were performed. A heatmap was generated from the Pearson correlation matrixes. \*Significant correlations ( $P < .05$ ;  $n = 5/\text{group}$ ).

## CONCLUSIONS

In the present study, we have introduced a practical murine model of iliac AVF placement that facilitates the examination of AVF-associated limb pathophysiology. Coupled with adenine-induced renal dysfunction, this model revealed several clinically relevant features, including patent AVF formation with altered limb hemodynamics, mild ischemia, and muscle mitochondrial dysfunction. Compared with previous AVF models, which used the central vasculature, the presented model provides investigators with the ability to interrogate the underlying biologic mechanisms of hemodialysis ARHD. This model can serve as a valuable tool to facilitate pre-clinical therapeutic development aimed at reducing the incidence and severity of hand disability after AVF placement.

## AUTHOR CONTRIBUTIONS

Conception and design: KK, EA, GL, SB, TR, SS  
 Analysis and interpretation: KK, EA, AM, TC, KH, KO, TR, SS  
 Data collection: KK, EA, QH, TC, KH  
 Writing the article: KK, EA, TR, SS  
 Critical revision of the article: KK, EA, AM, QH, TC, KH, KO, GL, SB, TR, SS  
 Final approval of the article: KK, EA, AM, QH, TC, KH, KO, GL, SB, TR, SS  
 Statistical analysis: Not applicable  
 Obtained funding: SS  
 Overall responsibility: SS  
 KK and EA contributed equally to this article and share co-first authorship.

## REFERENCES

- Johansen KL, Chertow GM, Foley RN, Gilbertson DT, Herzog CA, Ishani A, et al. US renal data system 2020 annual data report: epidemiology of kidney disease in the United States. *Am J Kidney Dis* 2021;77(Suppl 1):A7-8.
- Rehfuß JP, Berceci SA, Barbey SM, He Y, Kubilis PS, Beck AW, et al. The spectrum of hand dysfunction after hemodialysis fistula placement. *Kidney Int Rep* 2017;2:332-41.
- Scali ST, Chang CK, Raghinaru D, Daniels MJ, Beck AW, Feezor RJ, et al. Prediction of graft patency and mortality after distal revascularization and interval ligation for hemodialysis access-related hand ischemia. *J Vasc Surg* 2013;57:451-8.
- Goodkin DA, Bragg-Gresham JL, Koenig KG, Wolfe RA, Akiba T, Andreucci VE, et al. Association of comorbid conditions and mortality in hemodialysis patients in Europe, Japan, and the United States: the dialysis outcomes and practice patterns study (DOPPS). *J Am Soc Nephrol* 2003;14:3270-7.
- Berru FN, Gray SE, Thome T, Kumar RA, Salyers ZR, Coleman M, et al. Chronic kidney disease exacerbates ischemic limb myopathy in mice via altered mitochondrial energetics. *Sci Rep* 2019;9:15547.
- Thome T, Kumar RA, Burke SK, Khattry RB, Salyers ZR, Kelley RC, et al. Impaired muscle mitochondrial energetics is associated with uremic metabolite accumulation in chronic kidney disease. *JCI Insight* 2020;6:139826.
- Thome T, Salyers ZR, Kumar RA, Hahn D, Berru FN, Ferreira LF, et al. Uremic metabolites impair skeletal muscle mitochondrial energetics through disruption of the electron transport system and matrix dehydrogenase activity. *Am J Physiol Cell Physiol* 2019;317:C701-13.
- Gamboa JL, Billings FT IV, Bojanowski MT, Gilliam LA, Yu C, Roshanravan B, et al. Mitochondrial dysfunction and oxidative stress in patients with chronic kidney disease. *Physiol Rep* 2016;4:e12780.
- Gamboa JL, Roshanravan B, Towse T, Keller CA, Falck AM, Yu C, et al. Skeletal muscle mitochondrial dysfunction is present in patients with CKD before initiation of maintenance hemodialysis. *Clin J Am Soc Nephrol* 2020;15:926-36.
- Martinez Cantarin MP, Whitaker-Menezes D, Lin Z, Falkner B. Uremia induces adipose tissue inflammation and muscle mitochondrial dysfunction. *Nephrol Dial Transpl* 2017;32:943-51.
- Caplice NM, Wang S, Tracz M, Croatt AJ, Grande JP, Katusic ZS, et al. Neoangiogenesis and the presence of progenitor cells in the venous limb of an arteriovenous fistula in the rat. *Am J Physiol Renal Physiol* 2007;293:F470-5.
- Castier Y, Lehoux S, Hu Y, Foteinos G, Tedgui A, Xu Q. Characterization of neointima lesions associated with arteriovenous fistulas in a mouse model. *Kidney Int* 2006;70:315-20.
- Croatt AJ, Grande JP, Hernandez MC, Ackerman AW, Katusic ZS, Nath KA. Characterization of a model of an arteriovenous fistula in the rat: the effect of L-NAME. *Am J Pathol* 2010;176:2530-41.
- Guzman RJ, Krystkowiak A, Zarins CK. Early and sustained medial cell activation after aortocaval fistula creation in mice. *J Surg Res* 2002;108:112-21.
- Kojima T, Miyachi S, Sahara Y, Nakai K, Okamoto T, Hattori K, et al. The relationship between venous hypertension and expression of vascular endothelial growth factor: hemodynamic and immunohistochemical examinations in a rat venous hypertension model. *Surg Neurol* 2007;68:277-84; discussion: 284.
- Misra S, Fu AA, Anderson JL, Sethi S, Glockner JF, McKusick MA, et al. The rat femoral arteriovenous fistula model: increased expression of matrix metalloproteinase-2 and -9 at the venous stenosis. *J Vasc Interv Radiol* 2008;19:587-94.
- Nath KA, Kanakiriya SK, Grande JP, Croatt AJ, Katusic ZS. Increased venous proinflammatory gene expression and intimal hyperplasia in an aorto-caval fistula model in the rat. *Am J Pathol* 2003;162:2079-90.
- Yamamoto K, Protack CD, Tsuneki M, Hall MR, Wong DJ, Lu DY, et al. The mouse aortocaval fistula recapitulates human arteriovenous fistula maturation. *Am J Physiol Heart Circ Physiol* 2013;305:H1718-25.
- Yang ST, Rodriguez-Hernandez A, Walker EJ, Young WL, Su H, Lawton MT. Adult mouse venous hypertension model: common carotid artery to external jugular vein anastomosis. *J Vis Exp* 2015;27:50472.
- Dokun AO, Keum S, Hazarika S, Li Y, Lamonte GM, Wheeler F, et al. A quantitative trait locus (LSq-1) on mouse chromosome 7 is linked

- to the absence of tissue loss after surgical hindlimb ischemia. *Circulation* 2008;117:1207-15.
21. Li Y, Hazarika S, Xie D, Phippen AM, Kontos CD, Annex BH. In mice with type 2 diabetes, a vascular endothelial growth factor (VEGF)-activating transcription factor modulates VEGF signaling and induces therapeutic angiogenesis after hindlimb ischemia. *Diabetes* 2007;56:656-65.
  22. Khattri RB, Thome T, Ryan TE. Tissue-specific 1H-NMR metabolomic profiling in mice with adenine-induced chronic kidney disease. *Metabolites* 2021;11:45.
  23. Diwan V, Small D, Kauter K, Gobe GC, Brown L. Gender differences in adenine-induced chronic kidney disease and cardiovascular complications in rats. *Am J Physiol Renal Physiol* 2014;307:F1169-78.
  24. Kim K, Anderson EM, Thome T, Lu G, Salyers ZR, Cort TA, et al. Skeletal myopathy in CKD: a comparison of adenine-induced nephropathy and 5/6 nephrectomy models in mice. *Am J Physiol Renal Physiol* 2021;321:F106-19.
  25. Kasımay Ö, Şener C, Çakır B, Yüksel M, Çetinel Ş, Contuk C, et al. Estrogen protects against oxidative multiorgan damage in rats with chronic renal failure. *Ren Fail* 2009;31:711-25.
  26. Huber TS, Larive B, Imrey PB, Radeva MK, Kaufman JM, Kraiss LW, et al. Access-related hand ischemia and the hemodialysis fistula maturation study. *J Vasc Surg* 2016;64:1050-8.e1.
  27. Rieg T. A high-throughput method for measurement of glomerular filtration rate in conscious mice. *J Vis Exp* 2013;75:e50330.
  28. Qi Z, Whitt I, Mehta A, Jin J, Zhao M, Harris RC, et al. Serial determination of glomerular filtration rate in conscious mice using FITC-inulin clearance. *Am J Physiol Renal Physiol* 2004;286:F590-6.
  29. Ryan TE, Schmidt CA, Green TD, Spangenburg EE, Neuffer PD, McClung JM. Targeted expression of catalase to mitochondria protects against ischemic myopathy in high-fat diet-fed mice. *Diabetes* 2016;65:2553-68.
  30. Mayeuf-Louchart A, Hardy D, Thorel Q, Roux P, Gueniot L, Briand D, et al. MuscleJ: a high-content analysis method to study skeletal muscle with a new Fiji tool. *Skeletal Muscle* 2018;8:25.
  31. Kestenbaum B, Gamboa J, Liu S, Ali AS, Shankland E, Jue T, et al. Impaired skeletal muscle mitochondrial bioenergetics and physical performance in chronic kidney disease. *JCI Insight* 2020;5:e133289.
  32. Sato E, Mori T, Mishima E, Suzuki A, Sugawara S, Kurasawa N, et al. Metabolic alterations by indoxyl sulfate in skeletal muscle induce uremic sarcopenia in chronic kidney disease. *Sci Rep* 2016;6:36618.
  33. Su Z, Klein JD, Du J, Franch HA, Zhang L, Hassounah F, et al. Chronic kidney disease induces autophagy leading to dysfunction of mitochondria in skeletal muscle. *Am J Physiol Renal Physiol* 2017;312:F1128-40.
  34. Watson EL, Baker LA, Wilkinson TJ, Gould DW, Graham-Brown MP, Major RW, et al. Reductions in skeletal muscle mitochondrial mass are not restored following exercise training in patients with chronic kidney disease. *FASEB J* 2020;34:1755-67.
  35. Lok CE, Huber TS, Lee T, Shenoy S, Yevzlin AS, Abreo K, et al. KDOQI clinical practice guideline for vascular access: 2019 update. *Am J Kid Dis* 2020;75:S1-164.
  36. MacRae JM, Dipchand C, Oliver M, Moist L, Yilmaz S, Lok C, et al. Arteriovenous access: infection, neuropathy, and other complications. *Can J Kid Health Dis* 2016;3: 2054358116669127.
  37. Scali ST, Huber TS. Treatment strategies for access-related hand ischemia. *Semin Vasc Surg* 2011;24:128-36.
  38. Jia T, Olauson H, Lindberg K, Amin R, Edvardsson K, Lindholm B, et al. A novel model of adenine-induced tubulointerstitial nephropathy in mice. *BMC Nephrol* 2013;14:116.
  39. Kwei S, Stavrakis G, Takahas M, Taylor G, Folkman MJ, Gimbrone MA Jr, et al. Early adaptive responses of the vascular wall during venous arterialization in mice. *Am J Pathol* 2004;164:81-9.
  40. Yang B, Shergill U, Fu AA, Knudsen B, Misra S. The mouse arteriovenous fistula model. *J Vasc Interv Radiol* 2009;20:946-50.
  41. Kang L, Grande JP, Hillestad ML, Croatt AJ, Barry MA, Katusic ZS, et al. A new model of an arteriovenous fistula in chronic kidney disease in the mouse: beneficial effects of upregulated heme oxygenase-1. *Am J Physiol Renal Physiol* 2016;310:F466-76.
  42. Nath KA, O'Brien DR, Croatt AJ, Grande JP, Ackerman AW, Nath MC, et al. The murine dialysis fistula model exhibits a senescence phenotype: pathobiological mechanisms and therapeutic potential. *Am J Physiol Renal Physiol* 2018;315:F1493-9.
  43. Wang X, Chaudhry MA, Nie Y, Xie Z, Shapiro JI, Liu J. A mouse 5/6th nephrectomy model that induces experimental uremic cardiomyopathy. *J Vis Exp* 2017;129:55825.
  44. Wong CY, de Vries MR, Wang Y, van der Vorst JR, Vahrmeijer AL, van Zonneveld A-J, et al. A novel murine model of arteriovenous fistula failure: the surgical procedure in detail. *J Vis Exp* 2016;108:e53294.
  45. Krishnan AV, Kiernan MC. Uremic neuropathy: clinical features and new pathophysiological insights. *Muscle Nerve* 2007;35:273-90.
  46. Castaigne P, Cathala H-P, Beaussart-Boulengé L, Petrover M. Effect of ischaemia on peripheral nerve function in patients with chronic renal failure undergoing dialysis treatment. *J Neurol Neurosurg Psychiatry* 1972;35:631-7.
  47. Wodicka R, Isaacs J. Ischemic monomelic neuropathy. *J Hand Surg* 2010;35:842-3.
  48. Wilbourn AJ, Furlan AJ, Hulley W, Ruschhaupt W. Ischemic monomelic neuropathy. *Neurology* 1983;33:447-51.
  49. Kim K, Reid BA, Ro B, Casey CA, Song Q, Kuang S, et al. Heat therapy improves soleus muscle force in a model of ischemia-induced muscle damage. *J Appl Physiol* 2019;127:215-28.
  50. Ryan TE, Schmidt CA, Alleman RJ, Tsang AM, Green TD, Neuffer PD, et al. Mitochondrial therapy improves limb perfusion and myopathy following hindlimb ischemia. *J Mol Cell Cardiol* 2016;97:191-6.

Submitted Jul 16, 2021; accepted Sep 27, 2021.